



LAWRENCE
LIVERMORE
NATIONAL
LABORATORY

Radiation transport and energetics of laser-driven half-hohlraums at the National Ignition Facility

A. S. Moore, A. B. Cooper, M. B. Schneider, S. MacLaren, P. Graham, K. Lu, R. Seugling, J. Satcher, J. Klingmann, A. Comley, R. Marrs, M. May, K. Widmann, G. Glendinning, J. Castor, J. Sain, C. A. Back, J. Hund, K. Baker, W. W. Hsing, J. Foster, B. Young, P. Young

August 27, 2013

Physics of Plasmas

Disclaimer

This document was prepared as an account of work sponsored by an agency of the United States government. Neither the United States government nor Lawrence Livermore National Security, LLC, nor any of their employees makes any warranty, expressed or implied, or assumes any legal liability or responsibility for the accuracy, completeness, or usefulness of any information, apparatus, product, or process disclosed, or represents that its use would not infringe privately owned rights. Reference herein to any specific commercial product, process, or service by trade name, trademark, manufacturer, or otherwise does not necessarily constitute or imply its endorsement, recommendation, or favoring by the United States government or Lawrence Livermore National Security, LLC. The views and opinions of authors expressed herein do not necessarily state or reflect those of the United States government or Lawrence Livermore National Security, LLC, and shall not be used for advertising or product endorsement purposes.

Radiation transport and energetics of laser-driven half-hohlraums at the National Ignition Facility

A. S. Moore,¹ A. B. R. Cooper,² M. B. Schneider,² S. MacLaren,² P. Graham,¹ K. Lu,¹ R. Seugling,¹ J. Satcher,¹ J. Klingmann,¹ A. J. Comley,¹ R. Marrs,³ M. May,³ K. Widmann,³ G. Glendinning,³ J. Castor,³ J. Sain,³ C. A. Back,³ J. Hund,³ K. Baker,² W. W. Hsing,² J. Foster,¹ B. Young,² and P. Young²

¹*Directorate Science and Technology, AWE Aldermaston, Reading, RG7 4PR, United Kingdom^{a)}*

²*Lawrence Livermore National Laboratory, P.O. Box 808, Livermore, CA 94551-0808 USA*

³*General Atomics, San Diego CA 92121 USA*

(Dated: 10 March 2014)

Experiments that characterize and develop a high energy-density half-hohlraum platform for use in benchmarking radiation hydrodynamics models have been conducted at the National Ignition Facility (NIF). Results from the experiments are used to quantitatively compare with simulations of the radiation transported through an evolving plasma density structure, colloquially known as an N-wave. A half-hohlraum is heated by 80 NIF beams to a temperature of 240 eV. This creates a subsonic diffusive Marshak wave which propagates into a high atomic number Ta₂O₅ aerogel. The subsequent radiation transport through the aerogel and through slots cut into the aerogel layer is investigated. We describe a set of experiments that test the hohlraum performance and report on a range of x-ray measurements that absolutely quantify the energetics and radiation partition inside the target.

Keywords: Hohlraums, x-ray

I. INTRODUCTION

Understanding the radiation transport mechanisms and plasma dynamics in high-Z hohlraums is an important area of research owing to their use in many high energy-density laser experiments to create a Planckian soft x-ray radiation spectrum for use in driving a range of other physics experiments.¹ The conversion of laser energy into x-rays, despite the detrimental effects of conversion efficiency, considerably improves the uniformity with which a physics experiment can be heated and reduces the effect of high-energy particles produced in the laser-plasma interaction. The direct illumination of a high-Z hohlraum material by intense laser radiation ($I \sim 10^{14}$ – 10^{15} Wcm⁻²) results in the rapid ionization and heating of material. The expansion of this plasma over a typical ns-duration laser pulse causes a long scale-length plasma interaction wherein inverse bremsstrahlung heating causes laser energy to be absorbed leading up to the critical surface. The high-temperature thin, plasma layer created by this interaction re-emits x-radiation into the hohlraum cavity, which is in majority captured and re-absorbed owing to the geometry of the hohlraum. The many re-absorption and emission events of photons transiting the hohlraum, evenly re-distribute the laser energy into the plasma and radiation field and set the hohlraum radiation temperature.

In addition to creating a thermal plasma inside the cavity, energy from the high temperature interaction region is transported diffusively into the cool, high-density hohlraum wall or other physics package creating a steep

heat front. Application of the diffusion equation to this problem, under conditions of constant or power-law dependent temperature, yields an analytically approachable self-similar solution, which describes the shape and propagation characteristics of this radiative heat- or Marshak wave.² Such a mathematical description is not only readily applicable to hohlraums, but has relevance in other astrophysical situations including star-forming regions of cool, dense nebulae that are heated by neighboring stars.³ Even with the vast distances involved in such astrophysical phenomena, the photon scale-length in these more dense regions of gas and dust lead to regions in which the radiation transport is effectively diffusive.^{4,5} One such region is the dense Southern Pillars of the Carina Nebula where a number of very hot early-type stars illuminate non-uniform gas regions creating diffusive heat waves and shocks.⁶ Laboratory experiments provide a unique and controlled way to investigate this problem and validate simulations in a way that is relevant to astrophysical observations.

To study these phenomena we heat a simple cylindrical half-hohlraum through a laser entrance hole (LEH) at one end and cover the opposite end with a high-Z Ta₂O₅ aerogel. We diagnose the energetics of the plasma created inside the half-hohlraum through measurement of the absolute flux and spatial distribution of x-rays emitted through the LEH. By introducing slots into the aerogel layer we enable the study of energy transport through a radiatively diffusive plasma. When slots are cut into the aerogel, energy initially “free-streams out from the hohlraum through the open area and wall material from inside the slot is ablated causing the slot to fill with plasma. If this is allowed to evolve for sufficient time (several ns) then the ablated material stagnates and sufficient density fills the slot that the radiation from the hohlraum

^{a)}Electronic mail: alastair.moore@physics.org

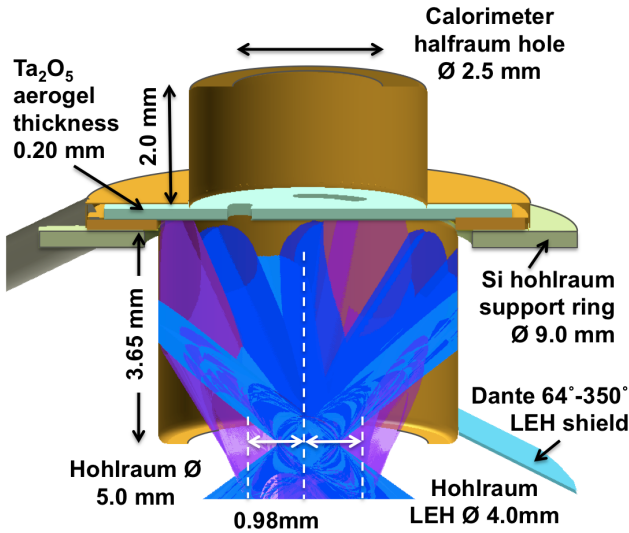


FIG. 1. Laser driven half-hohlraum and calorimeter halfraum target design. 30° laser beams are shown in purple, 44.5° in blue and 50° in light blue.

must diffuse through a number of optical depths (~ 10) to escape. An outward propagating shock propagates into the side of the slot creating a density structure that has been called an N-wave by some due to its resemblance to the letter “N”.^{7,8} In parallel to the energetics measurements presented here radiographic measurements of the shape of this density structure have been presented by Cooper et al..

II. EXPERIMENT DESIGN

In this paper we report on the first half-hohlraum or halfraum experiments to be heated using >100 kJ of 351 nm laser energy on the National Ignition Facility.¹⁰ The Au vacuum hohlraum had an inside diameter of 5.00 mm, was 3.85 mm in length, with a 4.00 mm laser entrance hole (LEH) and 50 μm wall thickness as shown in figure 1.

For measurements of the shock and Marshak wave propagation, a 150 μm thick, high-Z, nominally 500 mg/cc Ta_2O_5 aerogel covered the full aperture of the halfraum at the opposite end to the LEH. Experiments that studied energy transport through slots cut into the aerogel layer use a calorimeter halfraum attached above the aerogel layer to capture energy that flows through the slots. In these experiments a 200 μm thick aerogel covered the whole aperture, and 200 or 400 μm wide slots were cut into the aerogel either in an annular pattern with three supporting spokes or in a double “Y” pattern (see Fig. ?? below). The calorimeter halfraum extended 2.00 mm beyond the undriven side of the aerogel, was 4.00 mm diameter with a 2.5 mm diagnostic hole and the Au wall thickness was 25 μm .

The Ta_2O_5 aerogel was produced via a sol-gel pro-

cess that involves the hydrolysis of tantalum ethoxide $[\text{Ta}(\text{OC}_2\text{H}_5)_5]$ in an ethanol solution.¹¹ This method results in a porous structure with a characteristic grain size between 2 and 50 nm.¹² Accurate interpretation of the experimental data is critically reliant on knowledge of the Ta pentoxide aerogel under ‘as-shot’ conditions, and so the aerogel density and residual water content was characterized through gravimetric measurement and x-ray transmission measurements of machined aerogel billets.

X-ray transmission measurements using a Brehmsstrahlung, source (5-50 keV) with an Xradia MicroXCT system were carried out on all aerogel components prior to assembly into the hohlraum to quantify the density and uniformity of the Ta_2O_5 aerogel.¹³ Figure 2 shows the x-ray image of an aerogel with an annular slot (right) with three solid density Ta reference foils of thickness 1) $6.54 \pm 0.02 \mu\text{m}$, 2) $4.93 \pm 0.03 \mu\text{m}$, and 3) $4.06 \pm 0.02 \mu\text{m}$ to span the range of effective Ta thickness of the 500 mg/cc aerogel. The reference foils were independently calibrated between 4-6 keV using the National Synchrotron Light Source (NSLS) beamline X8A to cross-calibrate the thickness measurement.¹⁴

Adsorption of water molecules into the aerogel via both chemi- and physi-sorption significantly affects the material equation of state since the water molecules represent an additional energy sink. To quantify this each aerogel batch was characterized via two processes. Physisorption of water molecules results in a very weak (<0.5 eV) bond to Ta_2O_5 and so can be measured as a reduction in sample mass as the aerogel is put under vacuum. An average mass reduction of 2.2% ($\pm 0.5\%$) was found for all 22 aerogel batches measured. Secondly, elemental composition analysis performed under vacuum is used to measure the water molecules that remain in the sample under vacuum due to chemisorption. These results showed between 1 and 1.5 H_2O molecules for every Ta_2O_5 molecule remained after evacuating the sample. Consequently the chemisorbed mass of water present in the Ta_2O_5 aerogel under the ‘as-shot conditions is 4.4% ($\pm 1.7\%$). Using these measurements to calculate the cold opacity of the aerogel and water together with the Xradia calibrations and knowledge of the aerogel thickness, the density is measured to ± 5 mg/cc.

The target was held in the NIF target chamber with a stalk designed to reduce background x-ray emission due to the remnant 1053 nm and 527 nm unconverted light that propagates into the NIF chamber. On all shots the target was aligned vertically to $\pm 0.5^\circ$, so that the center of the LEH was at the center of the target chamber to within $\pm 30 \mu\text{m}$. Three cones of 351 nm laser beams that originated from the lower hemisphere of the chamber at 30°, 44.5° and 50° to the vertical axis irradiated the hohlraum. The 44.5° and 50° beams were pointed and focused to the center of the LEH and the 30° beams were focused in the LEH plane and pointed radially 0.98 mm from the hohlraum axis at their respective azimuthal

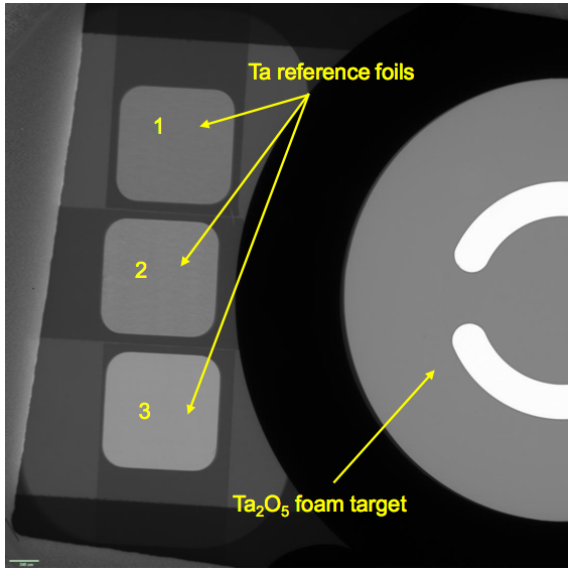


FIG. 2. Xradia image of Ta₂O₅ aerogel prior to assembly with hohlraum, with Ta reference foils of thickness: 1: 6.54 μm , 2: 4.93 μm , 3: 4.06 μm .

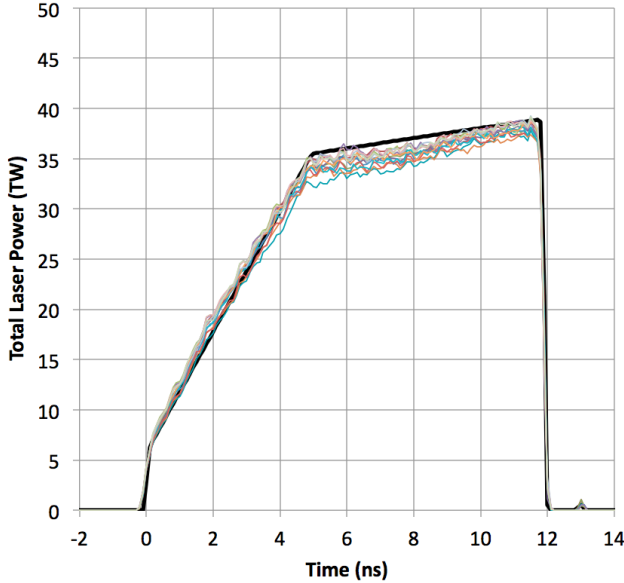


FIG. 3. Requested laser power (black) and laser power delivered to the half-hohlraum on 13 shots. The power is divided between the 80 NIF beams totaling 370 kJ.

angles (see Fig 1).

For initial shots a total of 240 kJ was delivered to the target by 80 laser beams in an 9 ns ramped laser pulse. 40% of the energy was delivered by each of the 44.5° and 50° cones, which each contain 32 beams in 8 quads; the 16 beams in the 30° cone delivered the remaining 20%. Later shots extended the length of the laser pulse to 12 ns so that the Marshak wave burned through the 200 μm of aerogel while the laser pulse was still heating the

hohlraum. This is shown in Figure 3, and this increased the total laser energy to 370 kJ. The laser energy from each quad was measured to $\pm 2\%$ accuracy. For all the experiments described, continuous phase plates (CPP's) were used to smooth the focal spot of each beam. In addition the 44.5° and 50° cones were smoothed by spectral dispersion at 45 GHz, and polarisation smoothing.¹⁶ Figure 3 illustrates the excellent shot-to-shot reproducibility of the laser pulse from thirteen shots together with the 12 ns requested pulse shape.

National Ignition Campaign CPP's (rev1 and rev 1a) were fielded in each of the different cones resulting in a spread of focal spot sizes. At best focus in the LEH plane the four beams from each quad overlap creating a spot with intensity of 1.6, 4.5 and 5.2 $\times 10^{14} \text{ Wcm}^{-2}$ from the 30°, 44.5° and 50° cones respectively. The peak laser intensity incident on the Au hohlraum wall was 1.6 $\times 10^{14} \text{ Wcm}^{-2}$. The laser power is divided between the 64 outer cone (44.5° and 50°) beams and the 16 inner cone (30°) beams such that the peak power on the inner cone beams is 90% of that on the outer cones. This slightly reduces the probability of significant energy clipping the edge of the hohlraum LEH, which is further reduced by removing SSD from the inner cone beams so that the focal spot size at the LEH is also reduced.

The half-hohlraum x-radiation that drives the radiation front into the Ta₂O₅ aerogel was measured using two techniques: 1) The x-ray power emitted from the hohlraum LEH was measured using a multi-channel soft x-ray power diagnostic Dante; this will be discussed in section III, 2) the velocity of a shock driven into an Al/Quartz sample that replaced the aerogel enabled the pressure history at the halfraum/aerogel plane to be directly measured; this is discussed elsewhere by Park et al.¹⁷ The x-ray energy transported through slots cut into the aerogel is characterized by measuring the temperature of the calorimeter halfraum and is described in section V.

III. HALFRAUM LEH X-RAY MEASUREMENTS

On all experiments an eighteen-channel soft x-ray power diagnostic Dante was used to measure the spectrum of x-rays emitted from the laser entrance hole.^{18,19} The Dante diagnostic measures the time-dependent x-ray emission over a range of photon energies from 50 eV to 20 keV. Each x-ray diode is filtered to measure a separate spectral region and is absolutely calibrated resulting in a 10% absolute error in x-ray flux for each diode depending on the x-ray photon energy range. 5% is attributed to statistical uncertainty in the measurement.

By combining multiple measurements at different photon energies to calculate the total x-ray flux, the resulting uncertainty in the absolute x-ray flux is reduced to 5%. If translated into a planckian radiation temperature this represents a 1σ uncertainty of 1.25%. One Dante fielded on the NIF is located at $(\theta - \phi) = (143^\circ - 274^\circ)$, looking

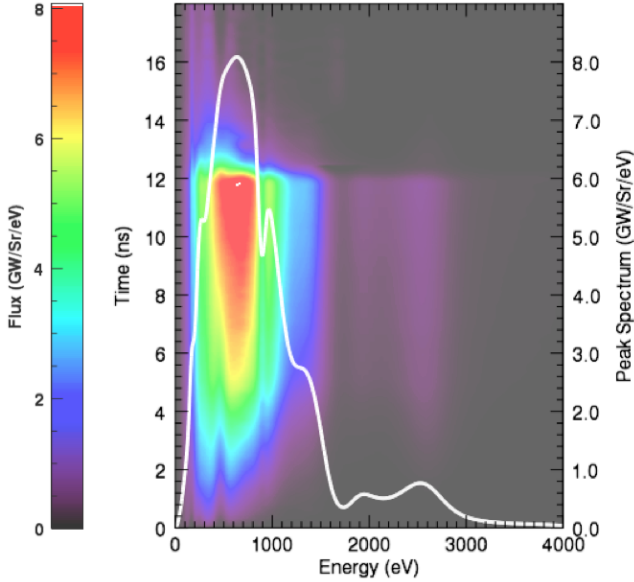


FIG. 4. Unfolded spectrum vs. time of x-ray emission from the half-hohlraum LEH measured by Dante 143°-274° for shot N110221-002-999. The spectrum at the time of peak flux is shown in white and is plotted on the left-hand axis.

into the LEH at 37° from the z-axis, a second is located at (64°-350°) in the upper hemisphere.

Two methods are used to calculate the x-ray flux emitted from the LEH: an iterative unfold and a matrix inversion algorithm. The iterative unfold code “UNSPEC” modifies an initial best-fit planckian spectrum using a series of Gaussian shapes representative of the spectral response function of the different x-ray diode diagnostic channels to best match the voltages measured by each of the x-ray diodes. The matrix inversion algorithm searches for the minimum basis set spectrum that matches the measured channel voltages within the error bars of each channel.²⁰ Figure 4 shows the spectrum predicted by the unfolding algorithm as a function of time (2D image) and at the time of peak emission (white line overlay). Both methods predict the voltages measured on each spectral channel of the diagnostic to within the error bars of each individual measurement, so have equal statistical significance, and as can be seen in Figure 5, the x-ray flux history calculated by both methods agree within the $1\sigma = 5\%$ error bars.

Figure 5(a) shows the total x-ray flux emitted through the LEH into the Dante diagnostic on a single shot (N110221-002-999) with post-shot simulations post-processed to calculate the Dante 143°-274° flux from the radiation hydrocodes LASNEX and NYM.^{21,22} Figure 5(b) shows the x-ray flux history for photon energies greater than 1.8 keV. This is a useful comparison for Au hohlraums because in addition to the Planckian tail it measures the M-band emission (2.3-3.3 keV) that is produced by the direct heating of Au by the laser spots on the hohlraum wall and the stagnation formed by the col-

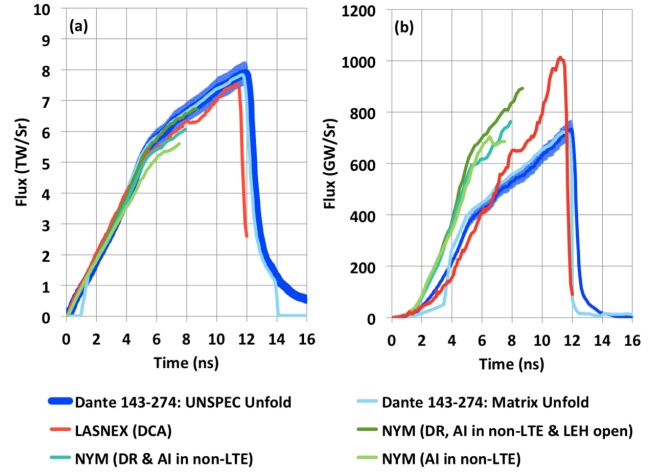


FIG. 5. (a) Total x-ray flux emitted from the half-hohlraum LEH measured by Dante 143°-274°, compared to simulations using NYM and LASNEX. (b) X-ray flux for photon energies >1.8 keV. DR: Dielectronic recombination; AI: auto-ionisation. The 5% absolute measurement error bars are shown on the UNSPEC unfold data.

liding Au plasma on the hohlraum axis; this can be seen in the spectrum in Figure 4

The M-band photons, having a greater mean free path, typically do not fully thermalize with the rest of the plasma and so this is a useful way to distinguish the performance of the simulations in calculating both the thermal and non-thermal spectral components.

The NYM simulations in Figure 5 are performed with and without dielectronic recombination (DR), and with an artificially open LEH, in which the Au cells at the LEH in the simulation are not allowed to move or expand into the open area of the LEH and block radiation emitted inside the hohlraum. Autoionization (AI) and DR can play an important role in calculating the atomic radiation processes involved with electron-ion collisions. AI resonant states can in particular contribute indirectly to the rates of excitation, ionization, and recombination which will affect the emitted radiation field.²³ The resonant DR process, in which an intermediate doubly-excited atomic state modifies the emitted photon energy from that of normal radiative recombination, plays an important role in determining the charge state balance, especially in non-hydrogenic systems, and so also has the ability to modify the emission spectrum from a hohlraum. These processes play a particularly important role in determining the balance between the thermal hohlraum emission and higher energy M-band photon flux since they are resonant processes that typically affect the detailed electronic configuration of the ions in the simulation.

The LASNEX simulations are performed using the detailed configuration accounting (DCA) atomic physics model which calculates the x-ray emission from many tens of atomic energy levels for non-LTE Au and includes both the DR and AI processes.²⁴ As can be seen from Fig-

ure 5 this also slightly underpredicts the total flux, and overpredicts the Au M-band photon emission.

Comparing the total flux calculated by the NYM simulations in Figure 5(a), it is clear that the addition of DR goes some way to improve the agreement with the data. Interestingly, all the simulations at early time < 5 ns are in good agreement with what is measured, and capture the rate of increase of the x-ray emission within the measured 1σ error bars. However, when the gradient of the laser pulse shape changes at 5 ns, the different simulations diverge. The additional calculation of DR resonant emission increases the total emitted flux by almost 0.5 TW/Sr at 8 ns, and to within 2σ of the data, but only by artificially holding the LEH open is the best agreement found. All the simulations over-predict the flux > 1.8 keV, shown in Figure 5(b), by between 200-300 GW/Sr at 8 ns, considerably outside the 5-10% uncertainty in the measurement of flux > 1.8 keV. Interestingly this shows no clear indication of changes to the higher-energy portion of the spectrum between simulations with and without DR within the noise of the simulation results.

Calculation of the internal hohlraum radiation temperature $T_r(t)$ from the x-ray flux measurements requires knowledge of the source size, i.e. LEH diameter, as a function of time:

$$T_r(t) = \frac{k}{e} \sqrt[4]{f(t) \frac{\int S(t)g(\Omega)d\Omega}{\sigma\pi r(t)^2 \cos(\theta)}} \quad (1)$$

where T_r is the temperature in eV, $S(t)$ is the measured x-ray flux [W/Sr], $g(\Omega)$ is the angular distribution of the emitted radiation, where $d\Omega$ is an element of solid angle [Sr], $r(t)$ is the source radius [m], $f(t)$ is the fraction of $S(t)$ emitted within $r(t)$, and θ the angle at which the source is viewed (37°). σ , k , and e are Stefan-Boltzmann constant [W/m²/K⁴], Boltzmann constant [J/K] and elementary charge [J/eV]. $g(\Omega)$ is typically assumed to be constant in time, and here is considered to be Lambertian since the hohlraum LEH is broadly equivalent to a uniformly emitting disc. In this case $\int S(t)g(\Omega)d\Omega = \pi S(t)$.

To investigate the spatial profile of emission within the hohlraum time-integrated x-ray images of the LEH were obtained using the lower NIF static x-ray imager (SXI-L) located at $(\theta - \phi) = (161^\circ - 326^\circ)$.²⁵ Consequently the SXI-L view into the hohlraum, being 19° from the hohlraum axis, is quite different to the 37° view of the Dante $143^\circ - 274^\circ$. The SXI-L image shown inset in Figure 6, was taken using a 2.0 magnification pinhole camera to image the laser-hohlraum interaction at approx. 5.0 keV. In National Ignition Campaign experiments described by Schneider et al. by using a combination of a static soft x-ray (800 eV) image and the hard x-ray image (~ 5.0 keV), it has been shown that an estimation of the shot-to-shot LEH closure can be obtained and used to correct the gas-filled ignition hohlraum temperature.^{26,27} Comparatively the vacuum hohlraum we describe here has a very different structure, and no soft-x-ray time-integrated im-

ages were available for this experiment. This image having quite a shallow view into the hohlraum shows three distinct bright regions of emission that result from the interaction of three of the four 30° quads of four beams with the Au hohlraum wall. In addition the somewhat brighter stagnation region on axis with the hohlraum can also be identified. Being time-integrated, the image is weighted towards the time of brightest emission occurring at the end of the laser-pulse. It is therefore also subject to movement in the interaction region between the laser and Au hohlraum wall which simulations show have moved radially inwards by $600 \mu\text{m}$ at 9 ns. Correction of the image to account for the 19° view allows the calculation of a radial average and comparison of this with horizontal line-out shows that these overlap at a diameter of 3.53 mm , shown by the white dashed line in the figure inset. Using this as a measure of the LEH diameter at the time of peak emission, the corrected Dante $143^\circ - 274^\circ$ peak temperature is calculated to be $236 \pm 4 \text{ eV}$. $T_r(t)$ calculated using a diameter of 3.53 mm is plotted in red in Figure 6, and can be compared to the radiation temperature calculated assuming that the LEH does not close (blue) which peaks at $220 \pm 3 \text{ eV}$. While this correction is somewhat arbitrary in that the diameter of 3.53 mm cannot be accurately related to a specific “edge” of the LEH, it is clearly a more accurate estimation of the internal hohlraum temperature than assuming the LEH does not evolve at all; it is also quite limited by the time-integrated and non-thermal ($\sim 5.0 \text{ keV}$) spectral nature of the SXI-L image.

To better constrain the hohlraum temperature an additional experiment was performed in which the hohlraum was rotated 180° about the equatorial plane and heated using the identical laser pulse delivered by the upper 30° , 45° and 50° laser beams. Soft x-ray ($< 1 \text{ keV}$) time-gated images were taken of the LEH towards the end of the laser pulse using a gated x-ray detector in DIM $0^\circ - 0^\circ$ looking directly down into the hohlraum perpendicular to the plane of the LEH. Using the combination of a 3° Au mirror and a light-tight $3.0 \mu\text{m}$ copper filter coated onto $1.0 \mu\text{m}$ parylene-N, the spectral response of the image was restricted to an approximate Gaussian centered at 900 eV and with a full-width at half maximum of approx. 60 eV . This mirror-filter selection was combined with a $1.0\times$ magnification pinhole-camera that used $30 \mu\text{m}$ diameter pinholes and was coupled to a gated x-ray detector with resolution $45 \mu\text{m}$ forming an imaging system with a resolution of $75 \mu\text{m}$.

Figure 7 shows the four images obtained of the LEH between 4.9 and 9.9 ns. More than $91.8 \pm 0.9\%$ of the emission was within the 4.0 mm diameter of the original LEH at all of the times measured, however it can be seen that the distribution of emission that is within the 4.0 mm diameter changes significantly. Circular overlays of increasing size are shown on each figure representing the diameter containing 25%, 50% and 75% of the total emission. These discrete measurements are used to recalculate the radiation temperature in Equation 1 with

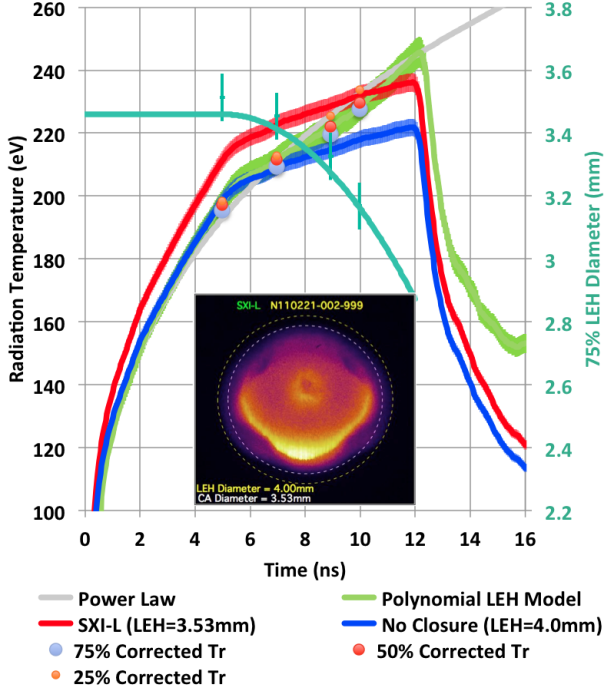


FIG. 6. Hohlraum temperature interpreted from the Dante 143° - 274° measurements calculated with no LEH closure (blue) and assuming an LEH of 3.53 mm based on the SXI-L clear aperture (red). Measurements of the LEH diameter containing 75% of the total emission are shown on the right-hand axis, and the temperature corrected using the 25, 50 and 75% emission diameters vs. time are also plotted. A power-law fit to the polynomial LEH model radiation temperature $T_r(t) = 125t^{0.27}$ is shown in grey. Inset: time-integrated SXI-L image at ~ 5.0 keV with 3.53mm clear aperture (CA) shown in white.

$f = 0.25, 0.5$ and 0.75 , at the four times shown in Figure 7. These are plotted in Figure 6 shown as blue, red and orange points. At any point in time these three corrections are in agreement since the largest standard deviation of the temperatures is 1.5%, which is within the 1.6-2.5% absolute uncertainty with which the temperature can be calculated given the 5% uncertainty in x-ray flux and $75 \mu\text{m}$ uncertainty in the measured diameter. Examining the circle containing 75% of the total emission, this decreases from a diameter of 3.51, to 3.45, 3.33 and finally 3.17 mm. If we assume a uniform radial distribution of emission at $t = 0$ ns, then the initial 75% diameter would be 3.46 mm, which when compared with the measurement in Figure 7(a) implies that there is little-to-no change in the emission size during the first 4.9 ns. Holding the initial diameter at 3.46 mm for the first 5 ns (equivalent to 75% of the initial 4 mm diameter) we fit a 2nd-order polynomial through the four data points shown on the right-hand axis in Figure 6. $T_r(t)$ is calculated from equation 1 with $r(t)$ from the polynomial fit to the $f=0.75$ data and plotted in green. At the time of peak temperature this correction is responsible

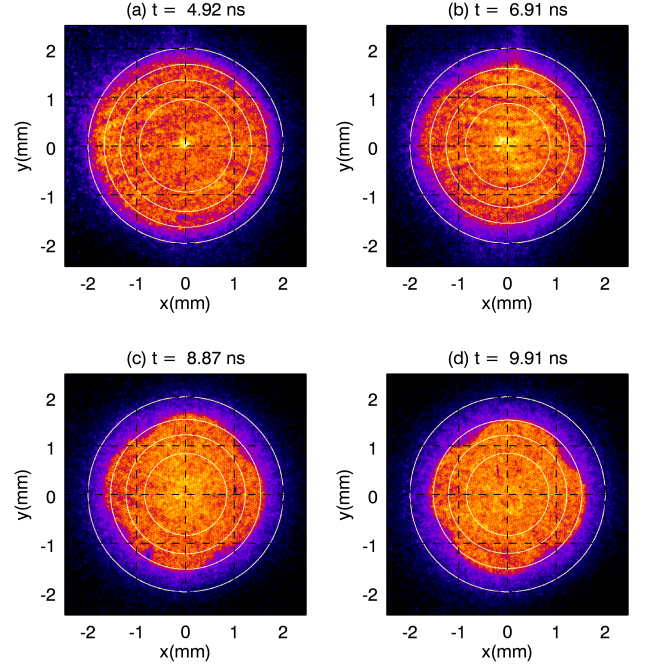


FIG. 7. Images of the emission through LEH at a photon energy of 900 eV at 4.92, 6.91, 97 and 9.91 ns. Circular overlays of increasing size indicate the diameter containing 25%, 50% and 75% of the emission. The largest circle represents the initial 4.0 mm diameter of the LEH.

for an approx. 20 eV ($\sim 9\%$) increase resulting in a peak radiation temperature of 240 ± 4 eV. This is in relatively close agreement with the SXI-L corrected temperature of 236 ± 4 eV, but it is clear that careful accounting of the time-dependent, radial distribution of emission through the hohlraum LEH is critical to a correct interpretation of the hohlraum radiation temperature.

As discussed in section II, the laser pulse was designed to create a radiation temperature that increased as a power-law in time. Utilizing the measured time-dependent LEH diameter to correct the radiation temperature shows that the pulse shape does indeed create such a power-law in time dependence as indicated by the grey line $T_r(t) = 125t^{0.27}$ in Figure 6.

Having calculated the internal hohlraum temperature using the LEH emission data this can be compared to the temperature calculated in the NYM and LASNEX simulations that were discussed earlier. Figure 8 shows the comparison of results from the same simulations as shown in Figure 5(a). Both NYM and LASNEX simulations bracket the radiation temperature calculated using the 75% emission diameter in Figure 7 and Figure 6. Both match the radiation temperature well during the first 5 ns, and only when the laser pulse flattens do the models diverge significantly in the same way as shown in the flux plots in Figure 5. It should be noted that the simulations post-processed to create a synthetic Dante 143° - 274° flux, plotted in Figure 5 are calculated by in-

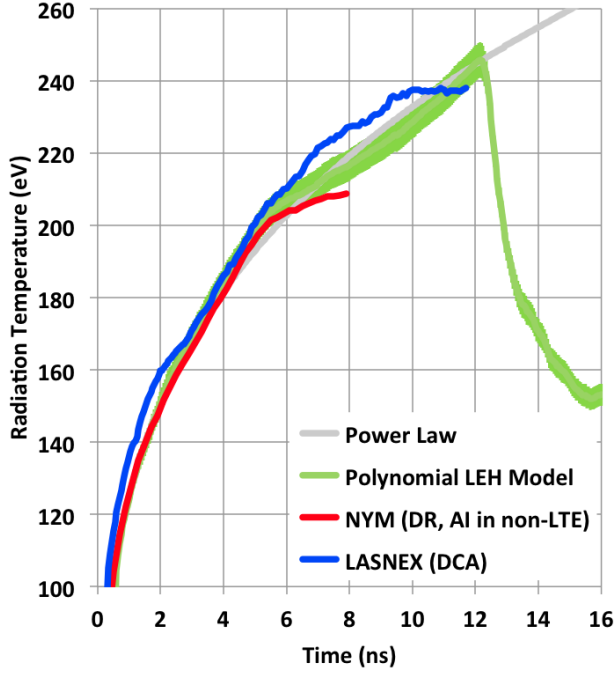


FIG. 8. Internal hohlraum temperature calculated using the polynomial fit to the LEH emission data compared to the internal temperature calculated by NYM and LASNEX from the same simulations as shown in Figure 5.

tegrating the flux between 0 and 13000 eV, while the temperatures shown in Figure 8, are extracted directly from the simulation and averaged over the region inside the hohlraum. Although both appear to diverge outside of the 1σ error bar plotted on the measured temperature, the maximum difference between either the simulation and the temperature inferred from the data is 10 eV. Based on the data in Figure 7, the closure of the LEH or decrease in the size of the emission region only begins after about 5 ns, and not during the initial ramp in the laser pulse. It is therefore most probable that the differences between data and simulations in inferred temperature and flux are related to the way that the motion of the plasma at the LEH is simulated and how this affects the amount of high density Au plasma that interacts directly with the laser pulse since it is the fraction of higher energy (>1.8 keV) radiation that is least well predicted by the simulations.

It is important to understand how the hohlraum energetics change as a function of laser energy since the radiation transport through the aerogel layer is a sensitive function of hohlraum temperature. Integrating the measured x-ray flux over time we calculate the x-ray energy per unit solid angle emitted through the LEH. Figure 9 shows this plotted against the 351 nm drive diagnostic (DrD) laser calorimeters that measured the laser energy directed into the hohlraum on 20 beamlines for each shot. Simulations performed in LASNEX indicate that the radiant x-ray energy per steradian emitted from the

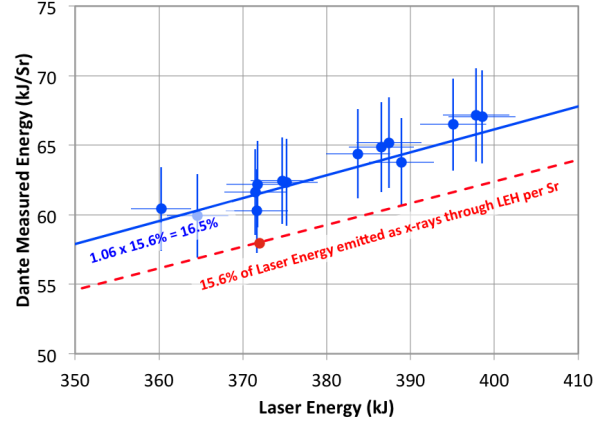


FIG. 9. Integrated x-ray energy emitted through the hohlraum LEH as a function of the incident laser energy compared to the trend from LASNEX simulations. Random error bars are plotted: 5% for Dante measured x-ray energy, and 0.5% for laser energy.

hohlraum is 15.6% of the incident laser energy scaling linearly. Comparatively, a simple linear fit to the measured data shows that approximately 6% more energy per unit solid angle, or 16.5%, is emitted through the LEH than in the simulations as expected from the plots in Figure 5(a). While the absolute energy is unsurprisingly different to simulations based on the results in Figure 5, it is clear that the trend expected from the simulations is reproduced to within 1%.

It is well-understood that any stimulated Raman (SRS) or Brillouin scattering (SBS) occurring in the coronal LEH plasma can decrease the laser energy that enters the hohlraum resulting in a decrease in hohlraum temperature. So to quantify the amount of backscattered energy, measurements of the SRS and SBS light were made on a number of shots using the full-aperture backscatter system (FABS) and near-backscatter imager (NBI) in beamlines 31B and 36B at 30° and 50° .²⁸ These measurements found less than 0.01% backscatter at 30° (0.8 J), and $<0.02\%$ at 50° (3.1 J) confirming that more than 99% of the incident 351 nm laser energy is absorbed in the halfraum.

In brief summary, simulations of the x-ray flux measured by Dante 143° - 274° using both NYM and LASNEX with a variety of atomic physics models seem to consistently over-predict the harder x-ray (>1.8 keV) emission attributed to the laser spots directly heating Au plasma, but under-predict the total x-ray flux emitted from the hohlraum LEH. However, when measurements of the spatial distribution of thermal 900eV x-ray emission from the LEH are applied to the measured flux the resulting internal hohlraum temperature is within $1-2\sigma$ of the predicted hohlraum temperature. This somewhat inconsistent picture is likely indicative of the limitations of (a) measuring the x-ray-flux at a single angle and assuming a Lambertian source, and (b) measuring the spatial uniformity of

the emission at a different angle to the flux measurement.

IV. CONSTRAINING Ta_2O_5 AEROGEL MATERIAL PROPERTIES

Accurate interpretation of all high energy density experiments requires constraining measurements of the material properties involved. In these experiments we constrain the equation of state and opacity of the Ta_2O_5 aerogel by diagnosing the shock and subsonic heat wave propagation through a uniform aerogel layer. Owing to the different dependencies of the shock and subsonic heat wave velocity on internal energy ϵ and Rosseland mean opacity κ , measurements of the shock and heat wave arrival time essentially form two simultaneous equations that can be used to independently constrain ϵ and κ .

The dependencies of the shock and heat wave on ϵ and κ can be understood by examining a textbook treatment of the problem. Hammer & Rosen found that by parameterizing κ and ϵ , as power-law functions of temperature and density, and restating the equation in terms of the mass variable $m = \int \rho dx$, where ρ is density, the problem becomes self-similar and a consistent solution for the ablated mass can be found for any power-law dependence of x-ray drive temperature as a function of time, $T(t) = T_0 t^k$.²⁹ This subsonic heat wave propagation theory was extended by MacLaren et al. to account for the rarefaction that forms once the shock has broken out of the rear surface.³⁰ The effect of the rarefaction is to enable the Marshak wave to travel significantly faster, due to the rarefied density, arriving at the back surface earlier than the infinite-slab analysis of Hammer & Rosen would predict. We summarize their results for our particular case of Ta_2O_5 which, after the rarefaction correction by MacLaren, show that the subsonic Marshak wave arrival time has the following dependencies:

$$t_{bt} \propto \left(\frac{\epsilon_0^{0.43} \kappa_0^{0.43} \rho_0 z}{T_0^{2.76}} \right)^{0.86} \quad (2)$$

where t is time, ρ_0 is the initial aerogel density and z is the slab thickness. ϵ_0 and κ_0 result from the parameterization of the internal energy and Rosseland mean opacity: $\frac{1}{\kappa} = \frac{1}{\kappa_0} T^\alpha \rho^{-\lambda}$, $\epsilon = \epsilon_0 T^\beta \rho^{-\mu}$.

The shock velocity can be calculated from the Rankine-Hugoniot shock relations and ablation pressure: $U_{shk} = \sqrt{\frac{2}{(\gamma+1)} \frac{P_{abl}}{\rho}}$ where γ is the adiabatic index. Hammer & Rosen present a detailed analytical derivation for the dependence of ablation pressure on the parameterized opacity and equation of state for a subsonic Marshak wave, the results of which are shown in Equation 3. The weak dependence of shock velocity on equation of state can be understood from simple dimensional considerations equating the flux absorbed within one optical depth ($\sigma T^4 / \rho \kappa x$) with the ablation pressure multiplied by the

sound speed $P_{abl} \sqrt{(\gamma-1)\epsilon}$ and solving for ablation pressure. The position of the heat front determines the volume of heated material behind the shock. As shown by Hammer and Rosen this is dependent on the inverse root of opacity and equation of state, and so in this simple approximation cancels with the $\sqrt{\epsilon}$ in the expression for sound speed leaving the ablation pressure dependent only on $\kappa^{-0.5}$. Following the more detailed analysis by Hammer & Rosen and fitting the Ta_2O_5 opacity and equation of state yields the dependence of shock front arrival time:

$$t_{shk} \propto \left(\frac{\kappa_0^{0.43} \rho_0 z^2}{\epsilon_0^{0.13} T_0^{2.76}} \right)^{0.42} \quad (3)$$

Examining equations 2 and 3 it is seen that since the arrival time of the shock is primarily dependent on the opacity κ_0 while the Marshak wave arrival time is dependent equally on the opacity and internal energy terms so used in conjunction ϵ and κ can both be constrained.

We measure t_{shk} and t_{bt} and compare directly with post-shot simulations tuning the opacity and equation of state to match the experimental data under the specific temperatures and densities we investigate. Re-arranging equations 2 and 3 to express the opacity and internal energy in terms of the other parameters, and then combining in quadrature the uncertainty contributions from the diagnostic timing (~ 50 ps), halfraum drive temperature (2%), and aerogel thickness (1%) and density (1%), it can be shown that the κ and ϵ can be constrained in a self-consistent manner to 16% and 22% respectively.

Measurements of t_{shk} and t_{bt} were made by measuring the x-ray flux emitted by the rear surface. To make these measurements the calorimeter halfraum shown in Figure 1 was removed, and a truncated 9 ns version of the laser pulse described in figure 3 was used to produce a 210 eV peak drive temperature measured through the hohlraum LEH. The soft x-ray emission was measured using the Dante soft x-ray power diagnostic positioned at $(\theta - \phi) = (64^\circ - 350^\circ)$, which has a view-angle of 64° to the normal of the aerogel surface.

This was configured to measure x-ray energy bands from 50 to 1000 eV, appropriate to accurately measure the cool <50 eV temperature emission from the Marshak wave as it breaks out of the aerogel surface. Nine measurements are made at different photon energies using identically configured x-ray diodes on two separate laser shots; the x-ray diode configurations including the full-width at half maximum (FWHM) of the gaussian fits to the response function are shown in Table I.

The low-temperature radiation (~ 10 eV) emitted by the shock arrival is visible only in the lowest energy channel, plotted in Figure 10. A consistent shock arrival time of 4.00 ± 0.15 ns is measured on both shots. Once the shock breaks out the rear surface of the aerogel, the surface begins to expand and rarefy, cooling somewhat and emitting less radiation until the arrival of the Marshak wave that can be seen at between 7.5 and 8.5 ns. The presence of water in the aerogel is observed in the Marshak wave arrival time. Post-shot LASNEX simulations

TABLE I. Dante 64°-350° diagnostic configuration for Marshak wave arrival time measurements, enabling absolute soft x-ray flux measurements in energy bands from 50-1000 eV.

Filter	Mirror	X-Ray Diode Cathode Material	Peak Energy (eV)	FWHM (eV)
Al 0.75 μm	7° B ₄ C	Cr	50	30
Si 1.0 μm	7° B ₄ C	Cr	70	40
B 0.2 μm^a	5° C	Al	140	60
Lexan 2.0 μm	3.5° SiO ₂	Al	230	70
Ti 1.0 μm	-	Al	390	60
V 1.0 μm	2.5° SiO ₂	Ni	450	80
Co 1.0 μm	-	Cr	700	80
Cu 1.2 μm	-	Cr	820	140
Zn 1.3 μm^a	-	Ni	940	100

^a filter is supported by a substrate of 0.4 μm CH.

of shot N090730 are post-processed to calculate the voltage predicted for the 0.75 μm Al channel and shown in Figure 10. Simulations using LEOS 2280 without water predict the sharp rise indicating the heat front arrival at approx. 7 ns about 600 ps earlier than the data. Only once 5% (by weight) water content is included, which is within the error bar of the measured $4.4 \pm 1.7\%$ water, is a good match between the simulation and data achieved.

The unfolded x-ray flux emitted as the Marshak wave burns through the aerogel is shown in Figure 11. Pre-shot density characterization indicated that the aerogel on both shots was 535 mg/cc - an equivalent optical depth to 5 μm of solid density Ta. The laser energy incident into the hohlraum on the two shots was 237.7 ± 1.4 kJ for N090730 and 239.1 ± 6.3 kJ for N091201, the larger error bar on the second shot being a result of increased degradation of the disposable debris shields which leads to greater uncertainty in the laser energy reaching the target. Therefore within the error bars the laser energy for the two shots is the same, however the x-ray flux measured by the Dante 143°-274° indicates that the integrated energy leaving the hohlraum through the LEH was 123.4 ± 6.2 kJ on N090730 and 114.4 ± 5.7 kJ on N091201. This $7.4 \pm 3.0\%$ decrease implies that the degraded transmission of the debris shields actually resulted in a lower laser drive on N091201 than indicated by the calorimeter measurements. Equation 2 tells us that the burnthrough time is proportional to $1/T^{2.37}$ and therefore a 1% decrease in drive temperature corresponds to a 2.37% increase in the burnthrough time. Since the hohlraum x-ray flux is proportional to σT^4 , a 2.37% earlier burnthrough time would be expected for a 4% increase in the measured x-ray energy in the hohlraum. The $4.7 \pm 3.6\%$ later arrival of the radiation heat front at 8.90 ± 0.15 ns on shot N091201 compared to 8.50 ± 0.15 ns on shot N090730 is therefore consistent with the degraded x-ray drive on N091201.

The planarity of the heat front was assessed through soft x-ray (<1 keV) time-gated images of the aerogel self-emission as the Marshak wave broke out. In a similar

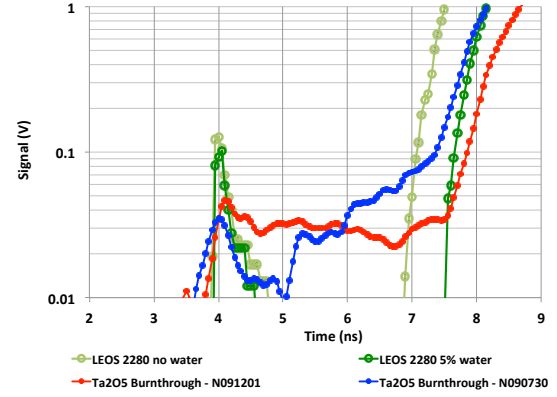


FIG. 10. Signal from the 50 eV (0.75 μm Al) Dante channel for the two 150 μm thick 535 mg/cc burnthrough shots. The shock breakout is visible in the Ta₂O₅ shots at 4.0 ± 0.15 ns. Post shot simulations for N090730 using the LEOS 2280 equation of state table for Ta₂O₅ are plotted in green, and must account for water present in the aerogel to agree with the data.

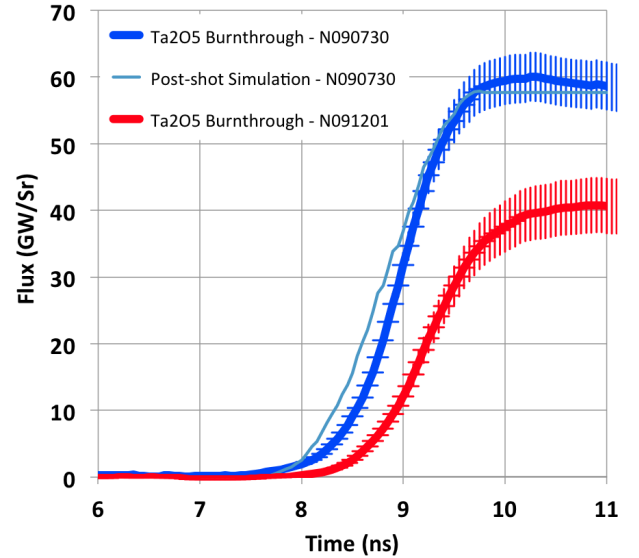


FIG. 11. X-ray flux emitted by the arriving heat front as it burns through the Ta₂O₅ aerogel; the delay in burnthrough emission for N091201 is explained by the degraded x-ray drive.

way to the LEH images shown in Figure 7, a 3° Nickel mirror and a light-tight 0.75 μm Aluminum filter coated onto 1.0 μm Parylene-N, are used to limit the spectral response of the image to an approximate Gaussian centred at 660 eV and with a full-width at half maximum of 250 eV. This mirror-filter selection was combined with a 1.0x magnification pinhole-camera and coupled to a gated x-ray detector to form an imaging system with resolution 100 μm .²⁷ A partial image is shown together with the pre-shot Xradia characterisation of the aerogel in Figure 12. It is clear from the radiograph that there are circu-

lar grooves that most likely originate from the machining process at varying radii through the aerogel. This has an effect on both the shock arriving at the rear surface and the radiation heat front. In detailed sub-scale NYM simulations of the aerogel that include the porous structure, no change in t_{shk} is observed, but a considerable decrease in the overall brightness of the shock front is seen compared to simulations that assume that the aerogel is a homogenous, low density medium - in good agreement with the results in Figure 10. This also tends to explain the heat front structure seen in Figure 12(b). Once the shock exits the rear surface the aerogel is accelerated, and this interface becomes classically unstable to the Rayleigh-Taylor instability.³² In the frame of the plasma being accelerated and unloading from the rear-surface of the aerogel, the comparatively high-density aerogel is “sitting on top of” the lower density ablated material expanding into the vacuum.

The growth rate competition of the density perturbations of different wavelength is an extensively studied topic and it is well-described that under ablative conditions the net growth factor is reduced by the flow across the interface. The subsonic Marshak wave that we describe here creates equivalent ablative-like conditions once the shock breaks out from the rear surface.³³ At this time the direction of flow at the rear surface is away from the material interface creating conditions stabilizing to perturbations. The net reduction in growth rate due to the ablation is most pronounced for the shortest wavelengths, so perturbations $<1 \mu\text{m}$ (of order the cell size of the aerogel) are stabilized and the longer wavelengths due to machining of the aerogel become dominant. Therefore by the time the heat front reaches the rear surface the larger machining perturbations remain as evidenced by the soft x-ray emission in Figure 12(b).

In brief summary we have shown how we can constrain the internal energy and opacity of Ta_2O_5 by measuring the arrival of the shock and subsonic heat front that results from being heated by the hohlraum described in III. Measurements of the heat front arrival time show this is dependent on accounting for the water present in the aerogel. Soft x-ray imaging helps to explain the reduced brightness of the shock due to the small-scale structure of the aerogel.

V. CALORIMETER HALFRAUM MEASUREMENTS

Slots were cut into the Ta_2O_5 aerogel to study energy transport through 3D and approximately 2D structures and investigate the scaling of energy transport with slot area. The slots were area-matched with identical widths of $200 \mu\text{m}$ and $400 \mu\text{m}$, details of the 2D and 3D slot geometries, which we label “3-smile” and “2-Y”, are shown in Figure 13.

The calorimeter halfraum placed on top of the aerogel angularly integrates the energy transported through the slots and by measuring the re-emission of the hal-

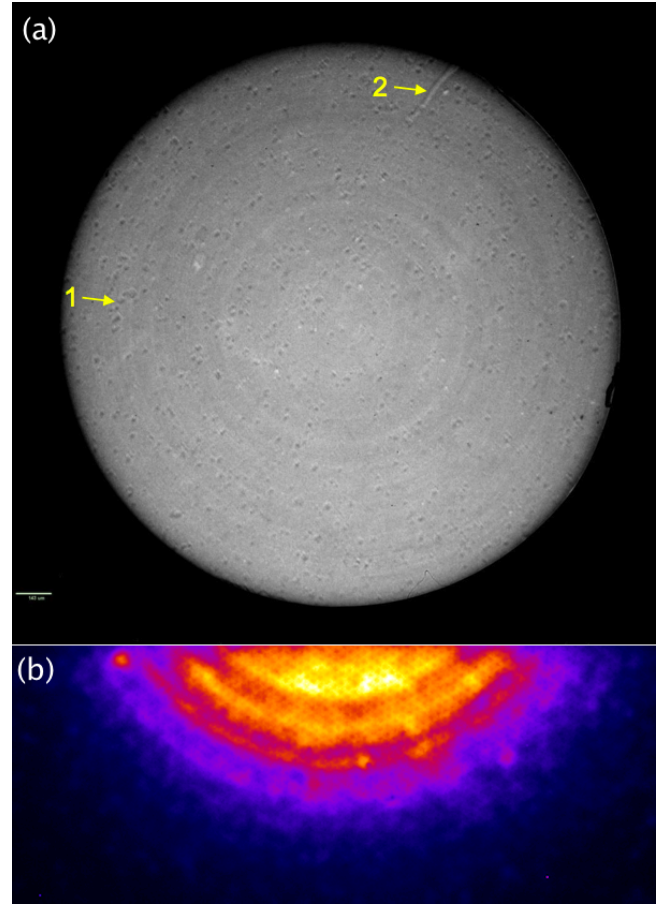


FIG. 12. (a) pre-shot Xradia radiograph ($>10 \text{ keV}$) of the Ta_2O_5 aerogel from shot N091201 (b) a 660 eV image of the heat front arrival at 8.65 ns .

fraum using the Dante $64^\circ\text{-}350^\circ >85\%$ of the 2π emission from the aerogel surface is captured. The spectral coverage of the instrument measured $>90\%$ of the flux emitted from the calorimeter. Since the energy transported through the slots in the Ta_2O_5 aerogel is re-emitted by the Au calorimeter, the flux measured by the Dante $64^\circ\text{-}350^\circ$ (F_{cal}) is dependent on both the radiation transported through the slots (F_{slot}), the ratio of re-emitted to absorbed flux in the Au or Au albedo (α_{Au}), and the calorimeter hole area, A_{hole} . Assuming a Lambertian or cosine dependence for the angular emission, the flux emitted from the calorimeter halfraum can be described by:

$$F_{cal} \left[\frac{GW}{Sr} \right] = \alpha_{Au}(T) F_{slot} \left[\frac{GW}{cm^2.Sr} \right] A_{hole} [cm^2] \cos(64^\circ) \quad (4)$$

Jones *et al.* have measured the low-temperature ($\sim 70 \text{ eV}$) albedo of Au. The results they present are in good agreement with LASNEX simulations and have an uncertainty of 11% .³⁴ The Au calorimeter halfraum we describe here spends a significant time at temperatures below 70 eV , and no data exists under these conditions.

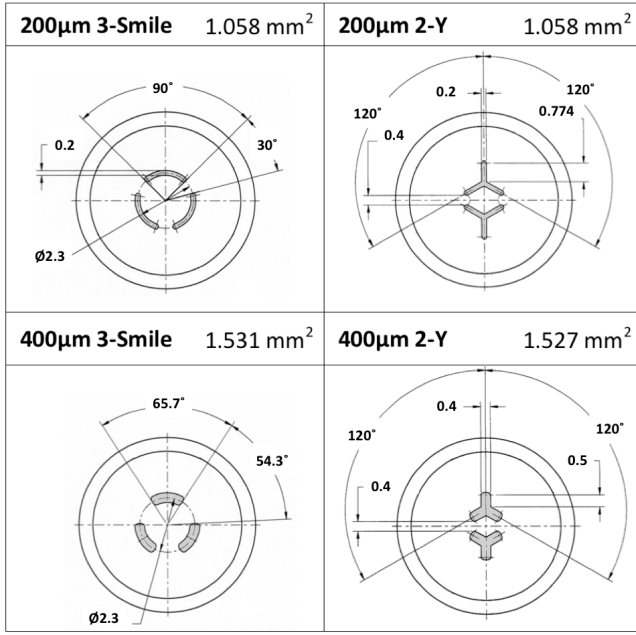


FIG. 13. 2D and 3D slot patterns (shown in grey) machined into the Ta_2O_5 aerogel substrate. All dimensions are in degrees and mm.

Furthermore, the albedo is a path-dependent variable, and therefore the albedo experienced at a specific time in these calorimeter halfraum experiments is dependent on the temperature evolution of the calorimeter halfraum wall up to that time. Experiments are planned to investigate this more carefully and will be the subject of future publications.

Important to all these measurements is the error bar assessment of the Dante 64° - 350° measurement at low flux. Here we discuss the relative and absolute error bars separately. For direct comparisons between two experiments only the relative error bars are important since the configuration of electrical attenuators, serialized filters, mirrors and X-ray diodes used in the Dante 64° - 350° was carefully controlled. For example, for shots comparing the $400\text{ }\mu\text{m}$ 2-Y and $400\text{ }\mu\text{m}$ 3-Smile targets, identical Dante 64° - 350° components were used. Conversely for comparison between the data and post-shot simulations it is the absolute error that is important, and so it is necessary for the calibration data of all the components to be taken into account.

Analysis of the relative error bars is focused mainly on the electrical error in the measured voltages included in the flux unfold. As has been shown elsewhere the flux unfold iterates to match the measured voltages identically, and so for relative shot-to-shot comparisons introduces $<1\%$ uncertainty.³⁵ The electrical noise floor for the Dante 64° - 350° is $1\sigma = 15\text{ mV}$. Analysis of the typical voltages measured for this configuration, which incorporates multiple measurements from the different channels on each shot, demonstrates that the relative error bar due to electrical noise is $<1\%$ for fluxes $>3\text{ GW/Sr}$. The

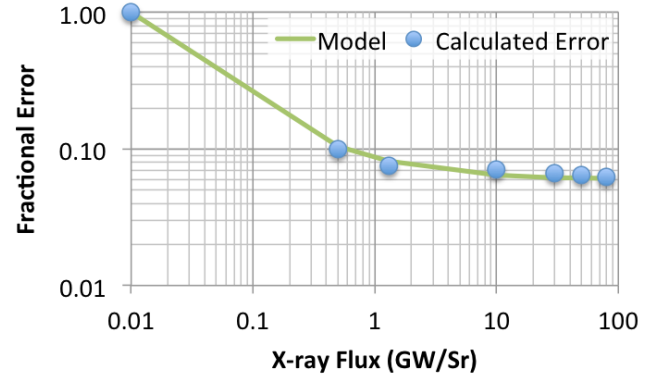


FIG. 14. Absolute error model for the calorimeter x-ray flux Dante measurements. The calculated root-sum errors for 1, 3, 4, 6, 8, 9 and 10 participating channels are plotted in blue with a functional fit in green $y = \exp(-1.8\ln(x)3.65) + 0.06$.

cross-timing of the multiple channels also affects the unfolded flux, and this has been demonstrated to be $<0.1\text{ ns}$ over a 20 ns window or $\sim 0.5\%$.

The absolute error is quantified by accounting for the calibration of all the individual components. X-ray filters, grazing incidence mirrors, x-ray diodes, signal cables, electrical attenuators, and oscilloscopes are carefully calibrated, referenced, tracked and archived for each shot. X-ray calibration of the individual components is performed at the NSLS.¹⁴ X-ray filter transmission is measured to better than $\pm 1\%$. Re-use of thin (few- μm) filters results in the gradual accumulation of debris sites - small $\sim \mu\text{m}$ -sized punctures in the filter - from the solid-density debris particles that are created by the energetic laser-target interaction. The use of multiple filters on one channel somewhat mitigates the effect of these debris sites since, once re-assembled, pinholes in multiple filters are unlikely to realign. All of these factors result in a combined uncertainty in the filter response for photon energies $< 1000\text{ eV}$ of 4-5%. The x-ray mirrors, depending on the grazing incidence angle, have an uncertainty in the reflectance of between ± 2 and 15%. The largest uncertainty component results from the uncertainty in the absolute sensitivity of the x-ray diodes. At the lowest photon energy measurable at NSLS (50 eV) this error is almost 20%, falling to less than 5% for photon energies above 500 eV . This is primarily dictated by the ability to self-calibrate the Si photo-diodes used at NSLS to provide a secondary standard. Finally, the aging of components, and change in sensitivity due to contamination products is estimated as approx. 8% based on over a decade of experience and re-calibration of used components. These uncertainties are assessed for each channel used in the measurement of the x-ray flux, and then the root-sum square divided by the square-root of the number of channels used in the flux unfold is assessed as the total 1σ flux uncertainty. As the x-ray flux increases a measurable signal is obtained on an increasing number of channels. This increased number of channels used to

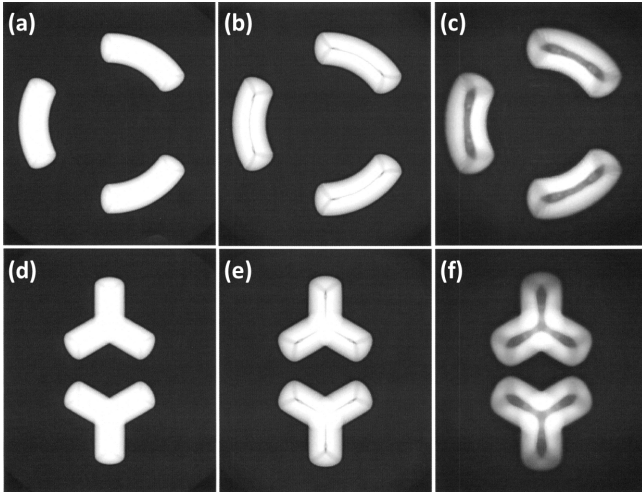


FIG. 15. Simulated radiographs of the evolving density structure inside the slots for the 3-smile and 2-Y patterns at 2ns (a) and (d), 4ns (b) and (e) and 6ns (c) and (f).

unfold the x-ray flux results in an overall decrease in the total uncertainty in x-ray flux. The discrete increases are shown as the blue points in Figure 14 together with a functional fit in green used to transcribe the error bars onto plots of the measured x-ray flux.

In brief summary, combining the uncertainty in the low-temperature Au albedo (11%) in quadrature with that of the Dante flux measurements indicates that at the lowest flux we can measure from the calorimeter halfraum (0.5GW/Sr - equivalent to a 30eV radiation temperature assuming our 2.0 mm calorimeter hole), we expect the 1σ uncertainty in the energy transported through the Ta₂O₅ aerogel to be 15%.

When the aerogel slot is first heated a shock begins to propagate into the material at the inside of the slot and for the first 3 ns radiation free-streams through the slot as the walls of the slot are ablated and the slot fills with plasma. Eventually (at about 6 ns for the 400 μ m slots) the plasma ablating from the walls of the slots collides and stagnates creating the “N” density structure across the width of the slot with shocks propagating into the undisturbed aerogel backed by a lower density ablation region and then a high density stagnation. This is termed an “N-wave” based on the similarity in conditions to the common solution to Burgers equation for two shocks with opposite phase¹⁵. As can be seen in the simulated radiographs in Figure 15(a) - (c), this density pattern forms slightly offset from center in the annular slots due to the different circumference of the inner and outer edge of the slot. Since the ablation rate is the same from the inner and outer slot edge, the stagnation forms slightly closer to the smaller radius slot-edge where the pressure of the two ablating plasmas balance; the streaked radiography experiments described by Cooper et al. demonstrate this fact.⁹

The curvature at the end of each slot results in an in-

teresting stagnation and “bubble” formation that can be seen in Figure 15(c) and (f). This occurs where the ablation perpendicular to the edge of the slot inside surface quickly stagnates at the “focus” of the slot end and owing to the higher pressure of ablation from the slot-end launches a blast-wave like feature along the central stagnation which is followed by a low density bubble. These end-effects introduce a perturbation to the 2D cylindrical interaction that occurs along the remainder of the slot, and so the number of ends (6) was kept the same between the area-matched 2D “3-smile” targets the 3D “2-Y” targets to minimise the effect of this perturbation. The initial slot open area was characterized using the Xradia radiographs to $\pm 0.001 \text{ mm}^2$.

At the center of each ‘Y’ pattern the evolution of the plasma is different again due to the triangular region, where the three legs of each ‘Y’ pattern intersect. Here there are three opposing flows as ablated plasma moves away from the higher density plasma in each leg towards the center of the pattern. As can be seen in Figure 15(d) - (f) the larger distance from the edge to the center in this triangular intersection region results in a stagnation at the center of the Y with lower density, and surrounding the stagnation a lower average density in the triangular intersection that is predicted to allow more energy to flow from the hohlraum into the calorimeter halfraum. The two equilateral intersection triangles of the pre-shot target form 10.5% of the total slot area for the 400 μ m 2-Y and 3.8% of the area for the 200 μ m 2-Y.

The x-ray flux measured by the Dante 64°-350° is primarily compared to post-shot simulations, but it is also of interest to be able to measure the relative enhancement in radiation transported through different slot geometries. However, to make A-B comparisons between two shots and, for example, calculate the measured fraction increase in energy transported into the calorimeter for the 2-Y target compared to the 3-Smile, it is necessary to understand the dependence of the energy transport through the slot on the aerogel density and the laser energy. Equation 5 shows how the x-ray flux is corrected for the small differences in the measured laser energy, E_{meas} , measured aerogel density, ρ_{meas} , and the background x-ray flux, F_{bg} (defined below) on two separate shots.

$$F_{corr} = \left(F_{meas} - \frac{F_{bg} E_{meas}}{E_{bg}} \right) \frac{C_{drive} \left(\frac{E_{norm}}{E_{meas}} - 1 \right) + 1}{C_{\rho} \left(\frac{\rho_{norm}}{\rho_{meas}} - 1 \right) + 1} \quad (5)$$

C_{drive} and C_{ρ} are scale-factors on the laser energy and aerogel density necessary to be able to compare measurements from separate shots and thereby determine a relative increase or decrease in the x-ray flux transported through the slot pattern. E_{norm} , E_{meas} and E_{bg} are the laser energy normalised to (370 kJ), the laser energy measured on each shot and the laser energy on the shots used to measure the x-ray background; similarly ρ_{norm} and

ρ_{meas} are the aerogel density normalised to (500 mg/cc) and that of individual shots. Both scale factors were determined from a suite of LASNEX simulations. C_{drive} is found to be 1.5 for the 400 μm slots and 2.6 for 200 μm slots, while $C_\rho = 2.0$. The reason behind these scalings with drive energy and density can be, to some degree, understood through consideration of a simple physical argument which we describe in more detail in the Appendix.

F_{bg} was determined from two dedicated shots N110220-002-999 and N110306-001-999, which bracketed in date the other data presented here. On these shots the hole in the calorimeter halfraum was covered from the inside with a tight fitting 50 μm Au foil so none of the emission measured by Dante 64°-350° originated from inside the calorimeter. The background signal is a result of a number of external x-ray sources. Two such sources include: x-ray emission from the outside of the hohlraum created by scattered 351 nm laser light that results from debris on the disposable debris shield (DDS) in the final optics assembly (FOA), and plasma emission formed by the low intensity ($<10^{12} \text{ Wcm}^{-2}$) interaction of 527 nm unconverted light striking the Si support ring and stalk. This background was minimized by careful design of the target stalk to minimize emission in the line-of-sight of Dante 64°-350°, and utilizing previously unused DDSs at the beginning of the campaign to minimize light-scatter from debris sites. The Dante 64°-350° background, shown in Figure 16, was measured to be at most 20% of the smallest measured calorimeter flux (200 μm 3-Smile), while the standard deviation of the two measurements, once corrected for variation in laser energy, is less than the Dante 64°-350° measurement uncertainty at all times. Consequently shot-to-shot fluctuations in the background are below the measurement threshold and the measured x-ray background can be subtracted from each shot and only introduce an additional 1.5-2.5 % uncertainty in F_{corr} for the 400 μm and 200 μm targets respectively.

The background corrected x-ray flux measured from the calorimeter halfraum for the four types of 2D and 3D targets are shown in Figure 17. The experiments studying the transport through 400 μm slots were performed using the same truncated 9 ns laser pulse as used in the IV. Different stages of slot closure can be seen in the data: an initial free-streaming phase until approx. 6 ns, during which the flux monotonically increases following the rise in flux in the drive hohlraum, followed by an inflection in the flux transported into the calorimeter halfraum due to the increased densification in the slot when the ablating plasmas stagnate. After this point, there is a significant number of optical depths ~ 10 of material in the slot and the transport becomes dominantly diffusive, following a more linear increase in flux emission before the arrival of the Marshak wave at approximately 10.5 ns when the aerogel burns through.

In Figure 17(a) the 200 μm 3-smile and 2-Y targets are compared and the ratio plotted on the right-hand axis.

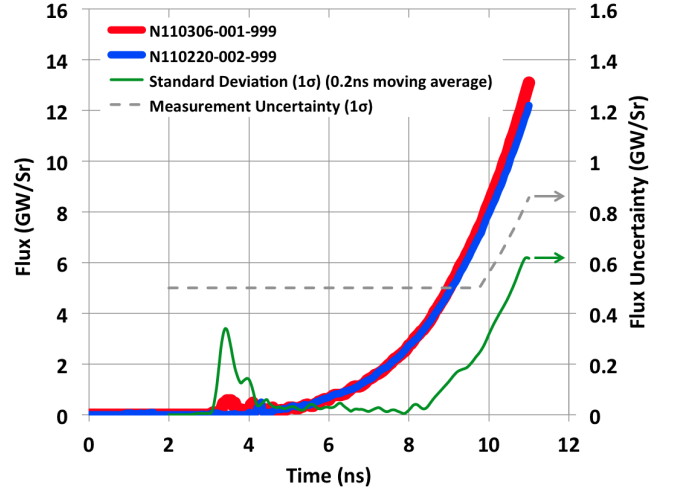


FIG. 16. Comparison between the two background shots taken at the beginning and end of the series of experiments to characterize the Dante 64°-350° x-ray background due to other x-ray sources external to the calorimeter hohlraum. The standard deviation of the two laser energy-normalized background results is less than the measurement uncertainty (7% for flux $> 6 \text{ GW/Sr}$) at all times between the two shots.

The ratio error bars reflect the relative uncertainties and do not include the errors due to calibration of components, where multiple measurements are available the average of the two is used in calculation of the ratio. This shows that for the 200 μm slot, there is a 7-9% enhancement in the radiation transported into the calorimeter once the transport is primarily diffusive (from 6-10 ns) due to the 3D intersection of the two 2-Y features. Comparatively, calorimeter hohlraum emission for the 400 μm slots is shown in Figure 17(b). The enhancement shown here is 12-15%. The large 1.2-1.25 ratio during the free-streaming phase (before 4 ns) is somewhat unexpected since the slot areas are matched. However during this early free-streaming phase, before the slots or calorimeter halfraum has begun to fill, the calorimeter halfraum wall of the 3D “2-Y” target has a greater view through the intersection of the laser spots interacting with the Au wall of the driven hohlraum, amplifying the radiation transported through the slots during the early free-streaming phase.

3D simulations were performed using the radiation hydrodynamics code KULL and using the opacity and LEOS 2280 equation of state models that account for the measured water content.³⁷ Figure 18 shows the drive and density corrected flux averaged where more than one shot exists, and in thin-lines, the simulations. The ratio of the simulations is plotted in green open circles. Since the data is compared to the simulations in an absolute sense, the error bars shown reflect the absolute calibration data, and are $\pm 5\%$ for flux $> 30 \text{ GW/Sr}$. The simulations are in good agreement with the data, agreeing within the error bars for $t < 4.5 \text{ ns}$. At times beyond this, the simula-

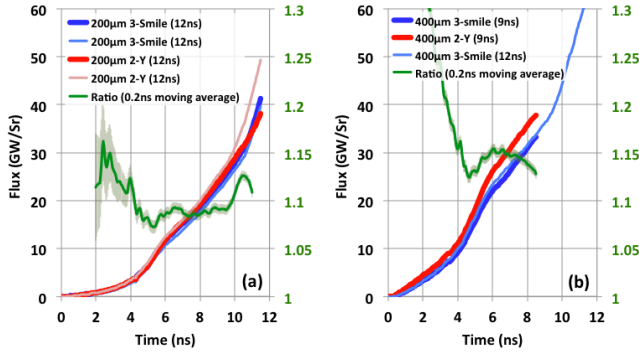


FIG. 17. (a) Background corrected calorimeter halfraum x-ray flux measured from targets with Ta_2O_5 aerogels machined with 200 μm slots; the ratio of 2-Y:3-Smile results are shown in green. Thick and thin lines represent data from separate repeat shots. (b) Background corrected calorimeter halfraum flux for 400 μm slots showing the enhanced radiation transport from the halfraum to the calorimeter through the 3D 2-Y target.

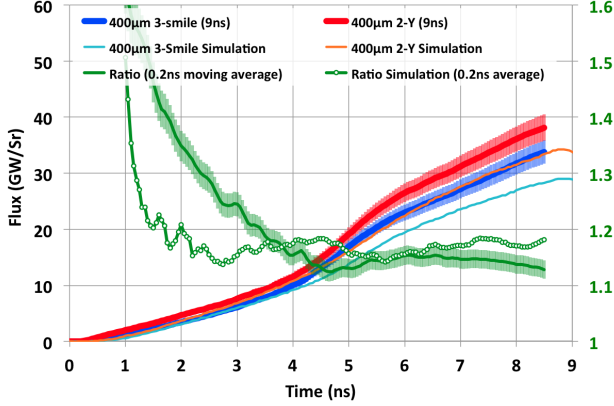


FIG. 18. Enhanced radiation transport through the 3D (2-Y) target compared with the more 2D (3-Smile) target. KULL simulations are compared with the measured calorimeter halfraum x-ray signal from two measurements of the 400 μm 3-Smile target and a single measurement of the 2-Y target. The absolute flux from simulations is slightly outside of the 1σ error bar, but the simulated flux ratio during the diffusive phase is in good agreement with the measurements.

tions under-predict the flux transported through into the calorimeter by up to 15% or 3σ at 8.5 ns. Integrating the x-ray flux in time shows that both for the 2-Y and 3-Smile target, the simulations under-predict the absolute energy emitted by the calorimeter by $11 \pm 1\%$. Contrary to this mis-match between the simulation and data, the ratio of the 400 μm 2-Y and 3-smile simulations agree with the data within the measured error bars during the diffusive phase ($t > 5$ ns) indicating that the way that the 3D intersection changes the diffusive energy transport is well-understood in the model. Interestingly the ratio during the free-streaming phase is somewhat under-predicted by the simulations.

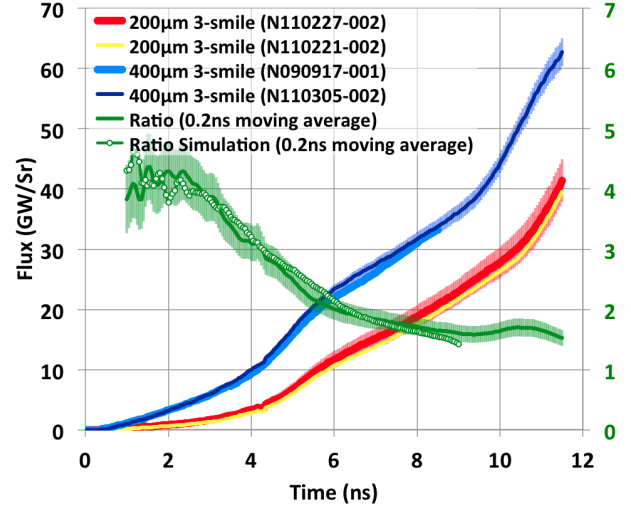


FIG. 19. Radiation transport through the 400 μm slot 2D (3-Smile) target measured on two shots, and compared to the equivalent 200 μm 2D target. The measured increase in flux transported through the 400 μm compared to the 200 μm target is well-matched by the simulations as shown by the plotted ratios.

The difference in energy transport between a 200 μm and 400 μm annular slot is shown in Figure 19. This highlights some of the non-linear behaviour of the slot closure. The ratio of the initial open area of the slots machined in to the Ta_2O_5 aerogel indicates that 1.45x more radiation would be transported through the 400 μm slot, than the 200 μm . Again the early-time behavior is dominated by the direct line-of-sight view seen by the calorimeter halfraum wall, which is well-simulated, but results in a greater increase in the x-ray flux transported at early-time than would be expected from a geometrical argument alone.

VI. CONCLUSIONS

We present a suite of measurements characterizing for the first time the hohlraum energetics, including radiation temperature and x-ray flux emitted from the LEH and x-radiation transport through a Ta_2O_5 layer, of a 3.65×5.0 mm hohlraum heated by a 370 kJ shaped laser pulse. The hohlraum and laser pulse, designed to create a power-law radiation temperature history at the aerogel interface, has been shown reach a peak radiation temperature of 240 ± 4 eV. Application of both time-integrated and dynamic LEH diameter measurements to correct the radiation temperature result in a good power-law in time temperature evolution. Simulations of the internal hohlraum temperature are in good agreement with this however some details, such as the flux of x-rays with energy $> 1.8\text{keV}$, do not agree with the data.

Using this half-hohlraum platform, measurements of

the shock and subsonic Marshak heat wave transit-time through a 150 μm Ta_2O_5 aerogel layer are used to constrain the material internal energy and opacity of Ta_2O_5 , by application of the analytical analysis described in detail by MacLaren et al..

Having constrained the material properties, we study the energy transported through 2D and 3D slot patterns machined into the aerogel providing a unique test-bed for radiation hydrodynamics codes. In particular we test the ability of the code to simulate the additional energy transported diffusively through the 3D intersection region of a Y-shaped slot compared to the energy transported through a 2D annulus of equivalent area. The energy transported is measured using calorimeter halfraum to capture $> 90\%$ solid angle and providing a highly constraining dataset. High fidelity 3D and 2D KULL simulations of the absolute energy transported through the slots compare favorably with the data being at worst within 2σ of the measured flux. However of particular significance is the simulated ratio of energy transported through the 2D and 3D features of equivalent area provide an excellent match to the data during the diffusive phase when plasma has filled the slot and the N-wave density structure has formed.

VII. ACKNOWLEDGEMENTS

We are grateful to the shot operations staff at the NIF. This work was jointly supported by the UK Ministry of Defence and was performed under the auspices of the US. Department of Energy by Lawrence Livermore National Laboratory under contract DE-AC52-07 nA273444. British Crown Copyright (2014). LLNL-JRNL-642974

VIII. APPENDIX

The dependence of flux transported into the calorimeter halfraum with either aerogel density or laser energy is important to understand if results from separate experiments, which may have small differences in these parameters, are to be compared directly without involving simulations. Here we present a simple discussion of how the scale factors C_{drive} and C_ρ can be determined from dimensional considerations that helps to elucidate the physical origin behind their values.

If we begin by considering that the only energy entering the calorimeter hohlraum is simply the time integral of the x-ray flux from the laser-driven hohlraum transmitted through the material filling the area of the slot, then we find:

$$E_{cal} = \int \sigma T(t)^4 \frac{A_{slot}(t)}{\rho(t)\kappa_R(T)z} dt \quad (6)$$

where $A_{slot}(t)$ is the time-dependent slot area, and $T(t)$ is the driven hohlraum temperature, $\rho(t)$ is the average density in the slot, κ_R is the Rosseland mean opacity and z is the thickness of the aerogel. The slot area increases with time as the plasma is ablated away from the inside edge, so the time-dependent slot area depends on the position of the heat front travelling laterally into the sides of the slot. Internal to the slot we can estimate the position of the ablative heat front (x), in the absence of significant hydrodynamic motion, and for a constant temperature drive:

$$x(t) \propto \sqrt{\frac{\sigma T^4 t}{\rho_0^2 \kappa_R \varepsilon}} \quad (7)$$

where ρ_0 is the density of the undisturbed aerogel. Assuming that the slot radius is sufficiently large that radial effects are small, the increase in area of the annular slot can be approximated by^{3,8}:

$$A_{slot}(t) \approx 2\pi r_0(w + 2x(t)) \propto \frac{T^2}{\rho_0} \quad (8)$$

where w is the initial slot width, and r_0 is the initial slot radius.

By performing a power-law fit of the Rosseland mean opacity of the Ta_2O_5 as a function of temperature and density we find that this scales primarily with only temperature as:

$$\kappa_R(T) \propto \frac{1}{T^2} \quad (9)$$

and so it can be shown that by inserting the dependencies in equations 8 and 9 into equation 6, the energy entering the calorimeter scales according to:

$$E_{cal} \propto \int \frac{\sigma T(t)^8}{\rho_0^2} dt \quad (10)$$

since $\rho(t) \propto \rho$. The x-ray flux lost from any driven hohlraum into the wall or aerogel layer typically scales with temperature according to T^n where $3 < n < 4$,³⁶ and so by substituting all these dependencies into the expression for the flux leaving the calorimeter halfraum yields the relationship:

$$F_{cal} = \alpha_{Au}(T) \frac{dE_{cal}}{dt} A_{hole} \cos(64^\circ) \propto \frac{F_{drive}^{8/n}}{\rho^2} \quad (11)$$

where F_{drive} is the hohlraum x-ray flux entering the aerogel layer and α_{Au} and A_{hole} are defined in equation 4. If we assume that small changes in energy entering the calorimeter do not significantly affect the Au albedo α_{Au} , then considering these dependencies separately we find the following approximate values for C_{drive} and C_ρ :

$$C_{drive} = \frac{\partial F_{cal}}{\partial F_{drive}} \approx 8/n = 2.0 - 2.7 \quad (12)$$

$$C_\rho = \frac{\partial F_{cal}}{\partial \rho} \approx 2 \quad (13)$$

which are in relatively good agreement with the results of the LASNEX simulations, which find C_{drive} is 1.5 for the 400 μm slots and 2.6 for 200 μm slots, while $C_\rho = 2.0$.

IX. REFERENCES

- ¹J. Lindl, Phys. Plasmas, 2, 3933 (1995).
- ²R. E. Marshak, Phys. Fluids, 1, 24 (1958).
- ³J. I. Castor *Radiation Hydrodynamics* Cambridge University Press (2004).
- ⁴J. H. Oort, L. Spitzer, Jr. Astrophys. J, 121, 6 (1955)
- ⁵T. Preibisch, V. Roccataliata, B. Gaczowski, T. Ratzka *Astronomy & Astrophysics*, 541, A132. (2012)
- ⁶N. Smith, M. S. Povich, B. A. Whitney, E. Churchwell, B. L. Babler, M. R. Meade, J. Bally, R. D. Gehrz, T. P. Robitaille, K. G. Stassun *Monthly Notices of the Royal Astronomical Society*, 406, 952. (2010)
- ⁷D. Mihalas, B. W. Mihalas *Foundations of Radiation Hydrodynamics*. Oxford University Press, New York. (1984)
- ⁸R. P. Drake, *Chapter 7: Radiation Hydrodynamics* in *High-Energy-Density Physics*. Springer. (2006)
- ⁹A. B. R. Cooper, M. B. Schneider, S. A. MacLaren, A. S. Moore, P. E. Young, W. W. Hsing, R. Seugling, M. E. Foord, J. D. Sain, M. J. May, R. E. Marrs, B. R. Maddox, K. Lu, K. Dodson, V. Smalyuk, P. Graham, J. M. Foster, C. A. Back, J. F. Hund *Phys. Plasmas*, 20, 033301 (2013)
- ¹⁰E. I. Moses, R. N. Boyd, B. A. Remington, C. J. Keane, R. Al-Ayat *Phys. Plasmas*, 16, 041006 (2009)
- ¹¹T. F. Baumann in *Handbook of Porous Solids*. Wiley-VCH, Weinheim (2002)
- ¹²J. E. Miller, T. R. Boehly, D. D. Meyerhofer, J. H. Eggert *Shock Compression of Condensed Matter*, 955, 71 (2007)
- ¹³A. Tkachuk, F. Duewer, H. Cui, M. Feser, S. Wang, W. Yun *Z. Kristallogr.*, 222, 650 (2007)
- ¹⁴R. J. Bartlett, W. J. Trela, F. D. Michaud, S. H. Southworth, R. W. Alkire, P. Roy, R. Rothe, P. J. Walsh, N. Shinn *Nuclear Instruments and Methods A*, 266, 199 (1988)
- ¹⁵G. B. Whitman *Linear and Nonlinear Waves*, Chapter 4. Pure & Applied Mathematics, Wiley-Interscience Publication (1974)
- ¹⁶C. A. Haynam, P. J. Wegner, J. M. Auerbach, M. W. Bowers, S. N. Dixit, G. V. Erbert, G. M. Heestand, M. A. Hennesian, M. R. Hermann, K. S. Jancaitis, K. R. Manes, C. D. Marshall, N. C. Mehta, J. Menapace, E. Moses, J. R. Murray, M. C. Nostrand, C. D. Orth, R. Patterson, R. A. Sacks, M. J. Shaw, M. Spaeth, S. B. Sutton, W. H. Williams, C. C. Widmayer, R. K. White, S. T. Yang, and B. M. Van Wronterghem *Applied Optics*, 46, 3276 (2007)
- ¹⁷H-S. Park, in prep. (2013)
- ¹⁸E. L. Dewald, K. M. Campbell, R. E. Turner, J. P. Holder, O. L. Landen, S. H. Glenzer, R. L. Kauffman, L. J. Suter, M. Landon, M. Rhodes, D. Lee *Rev. Sci. Instruments*, 75, 3759 (2004)
- ¹⁹J. L. Kline, S. H. Glenzer, R. E. Olson, L. J. Suter, K. Widmann, D. A. Callahan, S. N. Dixit, C. A. Thomas, D. E. Hinkel, E. A. Williams, A. S. Moore, J. Celeste, E. Dewald, W. W. Hsing, A. Warrick, J. Atherton, S. Azevedo, R. Beeler, R. Berger, A. Conder, L. Divol, C. A. Haynam, D. H. Kalantar, R. Kauffman, G. A. Kyralla, J. Kilkenny, J. Liebman, S. Le Pape, D. Larson, N. B. Meezan, P. Michel, J. Moody, M. D. Rosen, M. B. Schneider, B. Van Wronterghem, R. J. Wallace, B. K. Young, O. L. Landen, B. J. MacGowan *Physical Review Letters*, 106, 085003 (2010)
- ²⁰C. Thomas, in prep. (2013)
- ²¹G. B. Zimmerman, W. L. Kruer *Comments Plasma Phys Controlled Fusion*, 2, 51 (1975)
- ²²P. D. Roberts, S. J. Rose, P. C. Thompson, R. J. Wright *Journal of Physics D*, 13, 1957 (1980)
- ²³V. L. Jacobs *J. Quant. Spectrosc. Radiat. Transfer*, 54, 195 (1995)
- ²⁴H. Scott, S. Hansen *High Energy Density Physics*, 6, 39 (2010)
- ²⁵M. B. Schneider, O. S. Jones, N. B. Meezan, J. L. Milovich, R. P. Town, S. S. Alvarez, R. G. Beeler, D. K. Bradley, J. R. Celeste, S. N. Dixit, M. J. Edwards, M. J. Haugh, D. H. Kalantar, J. L. Kline, G. A. Kyralla, O. L. Landen, B. J. MacGowan, P. Michel, J. D. Moody, S. K. Oberhelman, K. W. Piston, M. J. Pivovarov, L. J. Suter, A. T. Teruya, C. A. Thomas, S. P. Vernon, A. L. Warrick, K. Widmann, R. D. Wood, and B. K. Young *Rev. Sci. Instruments*, 81, 10E538 (2010)
- ²⁶M. B. Schneider, N. B. Meezan, S. S. Alvarez, J. Alameda, S. Baker, P. M. Bell, D. K. Bradley, D. A. Callahan, J. R. Celeste, E. L. Dewald, S. N. Dixit, T. Dppner, D. C. Eder, M. J. Edwards, M. Fernandez-Perea, E. Gullikson, M. J. Haugh, S. Hau-Riege, W. Hsing, N. Izumi, O. S. Jones, D. H. Kalantar, J. D. Kilkenny, J. L. Kline, G. A. Kyralla, O. L. Landen, R. A. London, B. J. MacGowan, A. J. MacKinnon, T. J. Mccarville, J. L. Milovich, P. Mirkarimi, J. D. Moody, A. S. Moore, M. D. Myers, E. A. Palma, N. Palmer, M. J. Pivovarov, J. E. Ralph, J. Robinson, R. Soufli, L. J. Suter, A. T. Teruya, C. A. Thomas, R. P. Town, S. P. Vernon, K. Widmann, and B. K. Young *Rev. Sci. Instruments*, 83, 10E525 (2012)
- ²⁷F. Ze, R. L. Kauffman, J. D. Kilkenny, J. Wielwald, P. M. Bell, R. Hanks, J. Stewart, D. Dean, J. Bower, R. Wallace *Review of Scientific Instruments*, 63, 5124 (1992)
- ²⁸J. D. Moody, P. Datte, K. Krauter, E. Bond, P. A. Michel, S. H. Glenzer, L. Divol, C. Niemann, L. Suter, N. Meezan, B. J. MacGowan, R. Hibbard, R. London, J. Kilkenny, R. Wallace, J. L. Kline, K. Knittel, G. Frieders, B. Golick, G. Ross, K. Widmann, J. Jackson, S. Vernon, and T. Clancy *Review of Scientific Instruments*, 81, 10D921 (2010)
- ²⁹J. Hammer, M. D. Rosen *Physics of Plasmas*, 10, 1829 (2003)
- ³⁰S. MacLaren, in prep. (2013)
- ³¹J. Castor Private communication. (2010)
- ³²G. Taylor *Proceedings of the Royal Society of London A*, 201, 192. (1950)
- ³³J. D. Kilkenny, S. G. Glendinning, S. W. Haan, B. A. Hammel, J. D. Lindl, D. Munro, B. A. Remington, S. V. Weber, J. P. Knauer, and C. P. Verdon *Physics of Plasmas*, 1, 1379 (1994)
- ³⁴O. S. Jones, S. H. Glenzer, L. J. Suter, R. E. Turner, K. M. Campbell, E. L. Dewald, B. A. Hammel, J. H. Hammer, R. L. Kauffman, O. L. Landen, M. D. Rosen, R. J. Wallace, F. A. Weber *Physical Review Letters*, 93, 065002 (2004)
- ³⁵M. J. May, K. Widmann, C. Sorce, H.-S. Park, M. Schneider *Rev. Sci. Instruments*, 81, 10 e505 (2010)
- ³⁶M. D. Rosen *Office of Scientific and Technical Information Report ID: 109501; UCRL-JC-121585* (1995)
- ³⁷Rathkopf, J. A., Miller D. S., Owen, J. M., Stuart, L. M., Zika, M. R., *PHYSOR 2000 American Nuclear Society Topical Meeting on Advances in Reactor Physics and Mathematics and Computation into the Next Millennium Pittsburgh, PA May 7-11, 2000* (2000)